

Parallel Transport Time-Dependent Density Functional Theory Calculations with Hybrid Functional on Summit

Weile Jia
jiaweile@berkeley.edu
University of California, Berkeley
Berkeley, California

Lin-Wang Wang
lwwang@lbl.gov
Lawrence Berkeley National
Laboratory
Berkeley, California

Lin Lin*
linlin@math.berkeley.edu
University of California, Berkeley
Lawrence Berkeley National
Laboratory
Berkeley, California

ABSTRACT

Real-time time-dependent density functional theory (rt-TDDFT) with hybrid exchange-correlation functional has wide-ranging applications in chemistry and material science simulations. However, it can be thousands of times more expensive than a conventional ground state DFT simulation, hence is limited to small systems. In this paper, we accelerate hybrid functional rt-TDDFT calculations using the parallel transport gauge formalism, and the GPU implementation on Summit. Our implementation can efficiently scale to 786 GPUs for a large system with 1536 silicon atoms, and the wall clock time is only 1.5 hours per femtosecond. This unprecedented speed enables the simulation of large systems with more than 1000 atoms using rt-TDDFT and hybrid functional.

KEYWORDS

Time-dependent density functional theory, real-time, GPU, Non-equilibrium system, Hybrid exchange-correlation functional, Fock exchange operator

ACM Reference Format:

Weile Jia, Lin-Wang Wang, and Lin Lin. 2019. Parallel Transport Time-Dependent Density Functional Theory Calculations with Hybrid Functional on Summit. In *Proceedings of ACM Conference (submitted to SC'19)*. ACM, New York, NY, USA, 11 pages. <https://doi.org/10.1145/nmnnnnn.nmnnnnn>

1 INTRODUCTION

Real-time time-dependent density functional theory (rt-TDDFT) is one of the newest trends in electronic structure calculations [3, 27, 31, 33, 39]. Its popularity rises together with the recent experimental emphasis in electronic ultrafast phenomena in material science. It can be used to study ion collision, light absorption spectrum, laser-induced demagnetization and phase change, charge transfer, excited carrier dynamics, and chemical reactions. Rt-TDDFT will be even more powerful when it can be combined with the hybrid exchange-correlation functional [5, 28] within the density

functional theory (DFT). The hybrid functional mixes a fraction of the explicit Fock exchange integral with the semi-local exchange correlation functionals. It can be used to accurately describe the band gaps for a wide range of materials, especially with the recently developed range-separated hybrid functional [14, 15]. As a result, the rt-TDDFT + hybrid functional approach can be extremely powerful to describe, for example, the exciton excitation and charge transfer processes. Unfortunately, both rt-TDDFT and hybrid functional is extremely computational expensive compared to conventional ground state DFT calculations with semi-local functionals. In practice, rt-TDDFT can be hundreds of times slower than the conventional ground state molecular dynamics simulations due to the need for using small time step, hybrid functional can also be tens of times slower than the semi-local exchange correlation functional due to the evaluation of the Fock exchange term. As a result, planewave-based rt-TDDFT + hybrid functional simulations are rarely found in the literature, even for small systems, not to mention large ones with a thousand atoms. However, for many problems, e.g., for excited state charge transfer, large system simulation is essential. Besides, planewave basis is also important due to its flexibility, especially for excited states.

Fortunately, the situation has been improved due to both new algorithm developments and the emergence of new computer platforms like Summit (located in Oak Ridge National Laboratory, listed as No.1 supercomputer in the Top500 list in November 2018). The recently introduced parallel transport gauge formalism (PT) [1, 19] can increase the time step from the original sub-attosecond regime to around 50 attoseconds, while the Summit machine equipped with massive GPU processors has significantly increased the available computing power. Given this situation, it will be of paramount interest to test the limit of the rt-TDDFT+hybrid functional method on the Summit supercomputer. Given the heterogeneous architecture of the Summit (GPU+CPU), its latest hardware for data communication, and the large amount of total memory, the computer algorithms need to be adapted accordingly. Here, we show that, by implementing the new PT algorithm on GPUs, and by taking advantage of the large communication bandwidth and the large amount of memory on the machine, we can carry out an rt-TDDFT+hybrid functional simulation with the planewave basis set for a unprecedentedly large system with 1536 silicon atoms, with a practical time to solution of 1.5 hours per femtosecond on 768 GPUs.

We remark that in the context of ground state hybrid functional DFT calculations, several approaches have been proposed to reduce the cost. The application of the Fock exchange operator can be

*Corresponding author

Permission to make digital or hard copies of all or part of this work for personal or classroom use is granted without fee provided that copies are not made or distributed for profit or commercial advantage and that copies bear this notice and the full citation on the first page. Copyrights for components of this work owned by others than ACM must be honored. Abstracting with credit is permitted. To copy otherwise, or republish, to post on servers or to redistribute to lists, requires prior specific permission and/or a fee. Request permissions from permissions@acm.org.
submitted to SC'19, 2019.

© 2019 Association for Computing Machinery.
ACM ISBN 978-x-xxxx-xxxx-x/YY/MM... \$15.00
<https://doi.org/10.1145/nmnnnnn.nmnnnnn>

accelerated with a massive number of CPUs [9, 35]. The GPU acceleration has been reported in software packages such as ABINIT [11], BigDFT [29], NWChem [34], Octopus [4], PWmat [20, 21], Quantum ESPRESSO [30], VASP [12, 18], to name a few. When approximation of the Fock exchange operator can be tolerated, the cost can also be reduced through other algorithmic approaches such as localization [6–8, 38] and density fitting techniques [17].

Through our study, we like to address the following questions: (1) How scalable is the implementation, both in terms of strong scaling and weak scaling? (2) How large is the speedup comparing GPU with CPU, in the sense of the absolute fastest time to solution, and in the sense of the same power consumption? (3) What is the bottleneck in the most scalable case: computation or communication? (4) Whether the memory is a bottleneck? If not, what new algorithms one can use to take advantage of the large amount of memory? Through our study, we found that, the large capacity of the Summit machine allows us to implement some unique algorithms, such as the Anderson mixing for the wavefunctions, where up to 20 copies of wavefunctions are required; also the algorithm of the Fock exchange integral evaluations (Eq. 3 and Alg. 2), where a wavefunction is broadcast in an as-needed basis, and the computation can overlap with communication. The use of the new PT algorithm is essential. We show that the PT algorithm can be 20–30 times faster than the more conventional Runge-Kutta 4th order (RK4) method, and it can be efficiently implemented on supercomputers like Summit. The performance of the hardware also determines the choice of optimal algorithms. For example, recently it has been shown that in CPU machines, the adaptively compressed exchange (ACE) algorithm [24] can be combined with the PT formulation to reduce the time for rt-TDDFT + hybrid functional calculations [22]. In this work, we find that with the GPU acceleration, the use of the PT formulation alone leads to more efficient implementation on the Summit machine. We provide detailed performance analysis, which gives insights for how to implement similar electronic structure codes in such heterogeneous platforms, and what aspects of such platforms can be improved in the future to serve similar applications.

The rest of the manuscript is organized as follows. We review the algorithm for performing hybrid functional rt-TDDFT calculations with the parallel transport gauge formulation in section 2. The GPU implementation is shown in section 3. The setup of the test systems and the machine configuration are presented in section 4 and section 5, respectively. Then we show the numerical results in section 6, followed by the analysis in section 7 and conclusion in section 8.

2 PARALLEL TRANSPORT GAUGE FORMULATION OF RT-TDDFT

Real-time time-dependent density functional theory solves the following set of time-dependent equations

$$i\partial_t \Psi(t) = H(t, P(t))\Psi(t). \quad (1)$$

Here $\Psi(t) = [\psi_1(t), \dots, \psi_{N_e}(t)]$ is the collection of electron orbitals, and N_e is the number of electrons (spin degeneracy omitted). The time-dependent Hamiltonian takes the form

$$H(t, P(t)) = -\frac{1}{2}\Delta_{\mathbf{r}} + V_{\text{ext}}(t) + V_{\text{Hxc}}[P(t)] + V_X[P(t)]. \quad (2)$$

Here $V_{\text{ext}}(t)$ includes the contribution from the external field (such as the laser field), together with the local and nonlocal contribution from the pseudopotentials. The Hamiltonian also depends nonlinearly on the density matrix $P(t) = \Psi(t)\Psi^*(t)$. V_{Hxc} is a local operator and characterizes the Hartree contribution and the local and the semi-local part of the exchange-correlation contribution. The Fock exchange operator V_X is an integral operator with kernel $V_X[P](\mathbf{r}, \mathbf{r}') = -\alpha P(\mathbf{r}, \mathbf{r}')K(\mathbf{r} - \mathbf{r}')$. Here $K(\mathbf{r} - \mathbf{r}')$ is the kernel for the (possibly screened) electron-electron interaction [14, 15], and α is a mixing fraction.

In an rt-TDDFT simulation, the matrix-vector multiplication of the type $H[P]\Psi$ needs to be repeatedly performed. This is particularly the case for hybrid functional calculations, where each set of multiplications $V_X[P]\Psi$ requires the following operations:

$$(V_X[P]\psi_j)(\mathbf{r}) = -\sum_{i=1}^{N_e} \psi_i(\mathbf{r}, t) \int K(\mathbf{r} - \mathbf{r}') \psi_i^*(\mathbf{r}', t) \psi_j(\mathbf{r}') d\mathbf{r}'. \quad (3)$$

This amounts to solving N_e^2 Poisson-like equations. Due to the convolutional structure of K , this can be efficiently performed using the fast Fourier transform (FFT). In practice, the application of the Fock exchange operator usually takes about 95% of the total computation time.

The rt-TDDFT equation (1) can be equivalently expressed using a set of unitarily transformed orbitals. Physical observables such as the density matrix are by definition gauge-invariant. This allows us to seek for the optimal gauge for numerical simulation of rt-TDDFT. Recently, such optimal gauge has been identified [1, 19], which is defined implicitly through the following equation

$$i\partial_t \Psi = H\Psi - \Psi(\Psi^*H\Psi), \quad P(t) = \Psi(t)\Psi^*(t). \quad (4)$$

Here Ψ^* stands for the Hermitian conjugate of the matrix Ψ . Compared to Eq. (1), the only difference is the extra term $\Psi(\Psi^*H\Psi)$, which mixes the information from all orbitals together. The right-hand side of Eq. (4) is a residual type term. Its magnitude can be much smaller than $H\Psi$ on the right-hand side of Eq. (1), and the dynamics become smoother. In fact, $\Psi(t)$ solved from Eq. (1) can be viewed as the parallel transport (PT) of the initial wavefunctions to time t within the range of $P(t)$, and the corresponding implicitly defined gauge is called the parallel transport gauge. It can be proved that the parallel transport gauge yields the slowest possible dynamics among all possible choices of the gauge [19]. Coupled with implicit integrators such as the Crank-Nicolson scheme, the resulting PT-CN scheme solves the following nonlinear equation at each time step

$$\begin{aligned} & \Psi_{n+1} + i\frac{\Delta t}{2} \{H_{n+1}\Psi_{n+1} - \Psi_{n+1}(\Psi_{n+1}^*H_{n+1}\Psi_{n+1})\} \\ & = \Psi_n - i\frac{\Delta t}{2} \{H_n\Psi_n - \Psi_n(\Psi_n^*H_n\Psi_n)\}. \end{aligned} \quad (5)$$

Compared to explicit time integrators such as the explicit 4th order Runge-Kutta scheme (RK4) which often requires a sub-attosecond time step, the time step allowed by PT-CN can be significantly improved to around 10–50 attoseconds. This is particularly important for reducing the number of Fock exchange operator applications in hybrid functional calculations.

Alg. 1 summarizes the procedure for one step of time propagation using the PT-CN scheme. During each time step, we first evaluate

the initial residual R_n . The right-hand side of (5) can be viewed as propagating the wavefunctions by half a step. It is thus denoted by $\Psi_{n+\frac{1}{2}}$ and is fixed during the self-consistent field iteration. The new set of wavefunction Ψ_{n+1} needs to satisfy a fixed point problem and is denoted by Ψ_f during the iteration, and the residual for the fixed point problem is denoted by R_f . The fixed point problem is solved by the Anderson mixing method [2]. When the residual is sufficiently small, the SCF iteration can be terminated. In practice, we find that the SCF convergence can also be monitored by the convergence of the charge density.

Algorithm 1 One time propagation step with the PT-CN method.

INPUT: Ψ_n

OUTPUT: Ψ_{n+1}

- 1: Evaluate the initial residual $R_n = H_n \Psi_n - \Psi_n (\Psi_n^* H_n \Psi_n)$.
 - 2: Evaluate $\Psi_{n+\frac{1}{2}} = \Psi_n - \frac{i\Delta t}{2} R_n$, and let $\Psi_f = \Psi_{n+\frac{1}{2}}$.
 - 3: Evaluate the electron density ρ_f corresponding to Ψ_f .
 - 4: **for** $j = 1, 2, \dots$ **do**
 - 5: Update the potential and the Hamiltonian H_f .
 - 6: Evaluate the fixed point residual $R_f = \Psi_f + \frac{i\Delta t}{2} (H_f \Psi_f - \Psi_f (\Psi_f^* H_f \Psi_f)) - \Psi_{n+\frac{1}{2}}$.
 - 7: Perform Anderson mixing to update wavefunctions Ψ_f .
 - 8: Evaluate the electron density ρ_f corresponding to Ψ_f .
 - 9: If the change of the electron density is sufficiently small, exit the loop.
 - 10: **end for**
 - 11: Orthogonalize Ψ_f to obtain Ψ_{n+1} .
-

3 MULTI-GPU IMPLEMENTATION

In hybrid functional calculations with a planewave basis set, the application of the Fock exchange operator in the $H\Psi$ step often takes around 95% of the total computation time with a CPU implementation. However, according to Amdahl's law, in order to achieve a desirable speedup factor, almost all steps of the calculation needs to be accelerated using GPUs. Our implementation is based on PWDFT, which uses the planewave discretization and is an independent module of the massively parallel software package DGDFT (Discontinuous Galerkin Density Functional Theory) [16, 25]. In our implementation, all computationally intensive parts are performed using GPUs with either GPU-accelerated libraries or CUDA custom kernels. We also carefully overlap the MPI communication and GPU computation to take advantage of the heterogeneous architecture.

3.1 Hybrid parallelization scheme

There are two main parallel distribution schemes for the wavefunctions. The first one is the column based distribution scheme (also called the band index parallelization), i.e., each column of Ψ are distributed to different MPI tasks based on its band index (i.e. the column index). This data distribution scheme is highly efficient for the calculation of $H\Psi$. This is particularly the case for hybrid functional calculations since different MPI tasks are able to perform FFTs independently. The second one is the row based distribution scheme (also called the G -space parallelization, where G is a standard notation for the index in the Fourier space). In this scheme,

the data is distributed according to the partition of the Fourier coefficients. This distribution scheme facilitates the evaluation of matrix-matrix multiplications, such as the evaluation of the overlap matrix $S = \Psi^*(H\Psi)$ once $H\Psi$ is obtained.

In PWDFT, the wavefunctions Ψ are mostly distributed in the band index parallelization to evaluate the $H\Psi$ efficiently. The conversion from band index parallelization to G -space parallelization is performed via `MPI_Alltoallv` for matrix-matrix multiplication operations such as the evaluation of the overlap matrix, as shown in Fig. 1. Note that after the evaluation in the G -space, the wavefunctions are converted back to the band index parallelization format via `MPI_Alltoallv`. In this fashion, both $H\Psi$ and matrix-matrix multiplication operations can be evaluated efficiently. In the GPU implementation, the hybrid parallelization scheme plays an even more important role. This is because the band index parallelization allows us to use the CUFFT library for the $H\Psi$ calculation. However, the band index parallelization cannot scale to a large number of processors for matrix-matrix multiplications either on CPUs or GPUs, and we therefore need to convert to the G -space parallelization scheme. The hybrid parallelization scheme for the GPU implementation has been used in [36] for ground state electronic structure calculations. In the discussion above, we assume only the Γ point is considered for sampling the Brillouin zone. For solid state systems with k -point sampling, the wavefunctions can naturally be grouped according to the k -points, which adds an additional layer of parallelization.

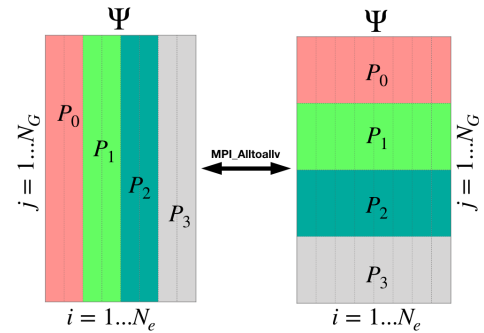


Figure 1: Illustration of the hybrid parallelization scheme with $N_e = 8$ wavefunctions on 4 MPI tasks. The number of planewaves N_G is usually on the order of $10^3 \sim 10^6$. Thus the maximum number of processes is limited by the N_e .

3.2 Evaluation of $H\Psi$

The cost of evaluating $H\Psi$ mainly consists of two parts: applying the Fock exchange operator and applying the pseudopotential.

The algorithm for applying the Fock exchange operator using a planewave discretization is shown in Alg. 2. The wavefunctions are distributed according to the band index. For a system with N_e wavefunctions and calculated on N_p processors, each processor holds $N_{e'} = N_e/N_p$ wavefunctions (assuming N_e is divisible by N_p). According to Eq. (3), each wavefunction Ψ_i needs to be multiplied to all other wavefunctions $\{\Psi\}_{j=1}^{N_e}$. This is performed using

an MPI_Bcast operation in line 3 of Alg. 2. Then each processor will solve the N_e Poisson-like equations with FFTs. Since each MPI task will eventually receive all N_e wavefunctions, the total communication volume is $N_p \times N_G \times N_e$ multiplied by the storage cost of a complex number, where N_G is the number of planewaves to store a wavefunction.

Algorithm 2 Applying the Fock exchange operator in $H\Psi$

INPUT: Wavefunctions Ψ distributed according to the band index.

OUTPUT: $V_X\Psi$ distributed according to the band index.

```

1: Let  $V_X\Psi$  be distributed according to the band index and initial-
   ized to zero.
2: for  $i = 1, N_e$  do
3:   if the current processor holds  $\Psi_i$  then
4:     Broadcast  $\Psi_i$  to all processors
5:   end if
6:   for  $j = 1, N_e$  do
7:     if the current processor holds  $\Psi_j$  then
8:       Solve Poisson-like equation using FFT with respect to
         the charge-like quantity  $\Psi_i^*(\mathbf{r})\Psi_j(\mathbf{r})$ , and add the solu-
         tion to  $(V_X\Psi)_j$ .
9:     end if
10:  end for
11: end for

```

In order to efficiently carry out Alg. 2 on GPUs, we perform a number of optimization steps.

1. *CUFFT and CUDA custom kernels (band-by-band)*. The first step of porting PWDFT onto GPU is to use the CUFFT library and CUDA custom kernels to accelerate the computation of Alg. 2. In this step, all relevant computation(from line 6 to line 10 in Alg. 2) are moved onto GPU in a band-by-band manner. In our implementation, the CUDA custom kernels are written to fill the gaps between the CUFFT calls, and there is no CPU-GPU synchronization during the computation. The CPUs are only used for performing MPI communication, and the data copy between CPU and GPU is necessary after the MPI_Bcast operation.

2. *Batched implementation*. Each V100 GPU on the Summit supercomputer has a peak performance of 7.8 TFLOPS and a peak bandwidth of 900 GB/s. The band-by-band implementation above cannot saturate the bandwidth of the GPUs. One way of improving GPU performance is to send more data to the GPU. In the GPU version of PWDFT, instead of sending the data $\Psi_i^*(\mathbf{r})\Psi_j(\mathbf{r})$ one by one, we batch them together and call a batched CUFFT. The corresponding CUDA custom kernels are also changed to a batched fashion. The batched version of code has two benefits: first it increases the computational intensity of the CUDA kernels to take advantage of the computing power of GPU; second, it reduces the latency between CPU and GPU by reducing the number of CUDA kernel launches.

3. *GPUDirect and CUDA-aware MPI*. On the Summit supercomputer, the IBM Spectrum CUDA-aware MPI is supported by hardware, which means inter-node GPUs can communicate with each other via MPI without explicitly copying data to the CPU. In PWDFT, we take advantage of this feature, and MPI communication is performed directly on the GPU data. In this step, the wavefunctions

are always kept on the GPU, and MPI_Bcast is performed using the CUDA-aware MPI in a band-by-band manner. This fine-grained (band-by-band MPI_Bcast) communication creates more opportunity to overlap the GPU computation and the MPI communication, since conceptually the CUDA-aware MPI and GPU computation can be performed simultaneously.

4. *Single precision MPI*. As will be seen later in the performance analysis, the MPI communication is mainly limited by the bandwidth of network adapters (NIC). To reduce the communication time of the Fock exchange operator applications, we use the single precision format for sending and receiving the wavefunctions, which reduces the communication volume by half. We also remark that the single precision format is only used in the MPI communication, which means wavefunctions will be converted back to the double precision format for computation. We find that this leads to negligible changes in the accuracy of the rt-TDDFT dynamics. This agrees with observations of ground state DFT calculations [10].

5. *Overlap computation and communication*. The last step of optimizing the Fock exchange operator calculation is to overlap the MPI communication and computation. Although theoretically CUDA-aware MPI communication overlaps with the GPU computation, we find that the MPI_Bcast and computation of the Fock exchange operator cannot be fully overlapped when the CUDA-aware MPI_Bcast is involved on Summit. Profiling of the Fock exchange part shows that there are two synchronized CPU-GPU memory copy operations in the communication step, as shown in Fig. 2. This is caused by the fact that the NIC is connected to the IBM POWER 9 socket as shown in Fig. 5. Thus MPI_Bcast will first copy the data from GPU to CPU, then the inter-node communication is performed over the NIC. This memory copy operation will introduce the CPU-GPU synchronization, thus the overlapping of computation and communication is disrupted. We get around this issue by performing an asynchronous CPU-GPU memory explicitly, followed by the MPI_Bcast using CPU instead of the CUDA-aware MPI. We remark that the CUDA-aware MPI are indeed used in other parts of the communication such as MPI_Alltoallv. Fig. 3 shows that the MPI communication and GPU computation can overlap perfectly, as the MPI communication time is entirely hidden behind the computation time. We stress that the overlapping is achieved based on the fact that CPU and GPUs can work independently, not on the unblocked MPI_Isend/MPI_Irecv communication. We have also implemented the round-robin communication strategy [29] via MPI_Send/MPI_Recv. We notice that the performance using the round-robin strategy and using MPI_Bcast is approximately the same on Summit. We also find that the round-robin strategy needs to be carefully implemented to be load-balanced. On the other hand, MPI_Bcast is a simpler strategy and takes advantage of the fat-tree interconnect topology of Summit.

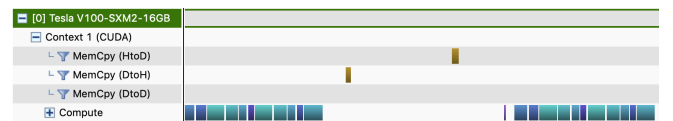


Figure 2: CUDA profiling reveals the implicit CPU-GPU synchronization introduced by the CUDA-aware Spectrum MPI.

Fig. 3 shows the reduction of the computational time associated with different stages of optimization. The testing system is a 1536 silicon atoms system, which will be discussed in section 4. The CPU version of PWDFT uses 3072 CPU cores (about 73 Summit nodes). The GPU version uses 72 GPUs (12 Summit nodes), and is around 7 times faster than the CPU version in terms of applying the Fock exchange operator.

Besides the application of the Fock exchange operator, we also apply the pseudopotentials to Ψ using the band index parallelization on GPU with CUFFT and CUDA custom kernels. In our implementation, we choose the real space representation for the nonlocal projectors, which can be stored as sparse vectors. This can often be more than 5 times faster compared to the reciprocal space implementation when the system size is more than a few hundred atoms [37]. In our current implementation, the entire set of local pseudopotentials and nonlocal projectors are stored on every processor. For the largest system tested in this paper with 1536 silicon atoms, the total memory cost for the nonlocal projectors is approximately 432MB. Each V100 GPU has its 16GB on-chip memory and is therefore sufficient. This simplified implementation allows us to apply the pseudopotentials without any communication cost, and thus fully takes advantage of the computational speed provided by the GPUs.

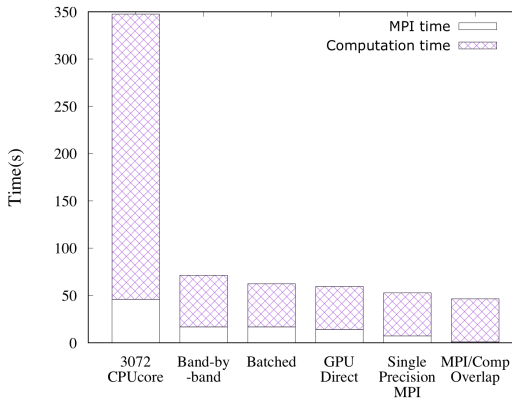


Figure 3: Wall clock time for applying the Fock exchange operator for a system with 1536 silicon atoms. The CPU version uses 3072 CPU cores, and the GPU version uses 72 GPUs.

3.3 Evaluation of the residuals

According to Alg. 1, there are two types of residuals to be evaluated in the PT-CN algorithm, denoted by R_n and R_f . For simplicity we only discuss the evaluation of R_f (Alg. 3); the evaluation of R_n is similar.

To calculate the residual R_f , the input data Ψ_f , $H_f\Psi_f$, and $\Psi_{n+\frac{1}{2}}$ are first converted from band index parallelization to G -space parallelization via an MPI_Alltoallv operation. Then the local overlap

matrix S can be evaluated on GPU by calling the CUBLAS matrix-matrix multiplication routine. Next, the local information from all processors is combined into the global overlap matrix using an MPI_Allreduce operation, followed by the rotation operation on GPU through a CUBLAS GEMM call. The residual is then calculated by BLAS-1 operations. Finally, the residual R_f will be transposed back to band index parallelization using an MPI_Alltoallv operation. In order to reduce the communication cost, the single precision format for R_f is used during the communication step using MPI_Alltoallv, and is then converted back to the double precision format during the computation step.

Algorithm 3 Algorithm of residual calculation.

INPUT: Wavefunctions Ψ_f , $H_f\Psi_f$, $\Psi_{n+\frac{1}{2}}$ distributed according to the band index.

OUTPUT: Residual P_i distributed according to the band index.

- 1: Use MPI_Alltoallv to convert Ψ_f , $H_f\Psi_f$, $\Psi_{n+\frac{1}{2}}$ to the G -space parallelization format.
 - 2: Evaluate the local overlap matrix $S_{\text{temp}} = \Psi_f^* H_f \Psi_f$
 - 3: Use MPI_Allreduce operation on S_{temp} to obtain the total overlap matrix S .
 - 4: Rotate the wavefunctions locally $\Psi_{\text{temp}} = \Psi_f S$
 - 5: Evaluate the residual $R_f = \Psi_f + \frac{i\Delta t}{2}(H_f\Psi_f - \Psi_{\text{temp}}) - \Psi_{n+\frac{1}{2}}$
 - 6: Use MPI_Alltoallv to convert R_f to the band index parallelization format.
-

3.4 Density Evaluation, Anderson mixing, wavefunction orthogonalization, and others

Because the wavefunctions are stored in the band index parallelization format, it is straightforward to evaluate the electron density $\rho(\mathbf{r}) = \sum_{i=1}^{N_e} |\psi_i(\mathbf{r})|^2$. This step requires representing the wavefunctions on a real space grid, which can be performed using FFTs, followed by an MPI_Allreduce operation across all MPI tasks. All above calculations are evaluated on the GPU, and the MPI_Allreduce operation is performed via CUDA-aware MPI.

The Anderson mixing method for solving the nonlinear equations requires the solution of a least squares problem for each wavefunction [2]. In our calculations, the maximum mixing dimension is set to 20. Thus after evaluating an overlap matrix with respect to the history of wavefunctions Ψ_f and the associated residuals R_f , the size of the least squares problem becomes very small, up to 20×20 . The main cost of the Anderson mixing is then due to the evaluation of overlap matrices that can be performed efficiently using the G -space parallelization.

Note that our implementation implies that up to 20 copies of the wavefunctions are needed for performing the Anderson mixing, which could be expensive if the wavefunctions are all stored on GPUs. However, we may store these wavefunctions on the CPU main memory, which has a large capacity of 512 GB on each computing node of Summit. During the computation, we copy all the wavefunctions corresponding to a single band i (up to $20 \times N_G$) from CPU to GPU, and the overlap matrices needed for the Anderson

mixing can be performed via CUBLAS matrix-matrix multiplications.

At the end of each rt-TDDFT time step, the wavefunctions Ψ will be re-orthogonalized. To improve the parallel efficiency, we again first evaluate an overlap matrix of the type $\Psi^*\Psi$ using the G -space parallelization. Then we can perform a Cholesky decomposition on the overlap matrix of size N_e , and rotate Ψ_f efficiently due to the G -space parallelization. The Cholesky decomposition is calculated on a single GPU with cuSOLVER library, and the subsequent rotation is performed via the GPU Trsm subroutine.

Besides the computationally intensive parts discussed above, all other operations such as the evaluation of the Hartree potential, the gradient of the electron density, the local part of the exchange-correlation potential, etc contributes to less than 2% of the computational time on CPUs. In the GPU version of PWDFT, these parts are all parallelized at the CPU level. For example, we parallelize the FFTs associated with the calculation of the gradient of electron density by using distributed FFTW in the Z direction. Such parallelization is important for the overall performance since all other computational intensive parts can be accelerated by up to 40 times on GPUs. We also keep the variables related to the charge density (such as the Hartree potential and the gradient of the electron density) on each MPI task. Hence MPI_AllGatherv and MPI_Bcast operation are performed after the computation.

4 SETUP OF THE TEST PHYSICAL SYSTEM

We report the efficiency of the GPU version of PWDFT using silicon systems ranging from 48 to 1536 atoms. The supercells are constructed from $1 \times 1 \times 3$ to $4 \times 6 \times 8$ unit cells, respectively, and each simple cubic unit cell consists of 8 silicon atoms with lattice constant being 5.43 \AA . In all the tests, the external potential is given by a laser pulse shown in Fig. ??(a), and its wavelength is 380nm. The total simulation time is 30 fs, and the time step using the PT-CN method is set to 50 as. Thus the total number of rt-TDDFT steps is 600. The stopping criteria is set to 1.0×10^{-6} for the electron density error. The average number of SCFs is 22 and the maximum Anderson mixing dimension is set to 20. We use the SG15 Optimized Norm-Conserving Vanderbilt (ONCV) pseudopotentials [13, 32] and HSE06 functionals [15] in all the following tests. The kinetic energy cutoff is set to 10 Hartree. For the system with 1536 atoms, the number of grid points for a wavefunction is $N_G = 60 \times 90 \times 120 = 648,000$. This corresponds to a charge density grid $120 \times 180 \times 240$. The Fock exchange operator is evaluated on the wavefunction grid. The number of occupied wavefunctions is 3072.

5 MACHINE CONFIGURATION

All numerical tests are performed on the Summit supercomputer. Fig. 5 shows the architecture of one of the 4608 Summit computing nodes. Each computing node consists of two identical groups, and each group has one IBM POWER 9 socket and 3 NVIDIA Volta V100 GPUs connected via NVLink with a bandwidth of 50GB/s. Each POWER socket has 22 physical CPU cores and share 256GB DDR4 CPU main memory, and each V100 GPU has its own 16GB high bandwidth memory. The CPU bandwidth is 135GB/s and GPU

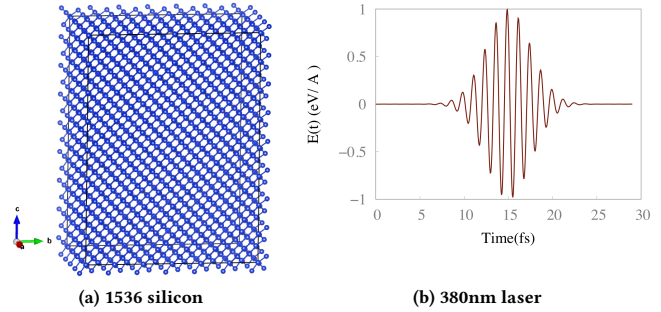


Figure 4: Atomic configuration and external laser field.

bandwidth is 900GB/s. Each GPU has a theoretical peak performance of 7.8 TFLOPS double precision operations. The two groups of hardware are connected via X-Bus with a 64GB/s bandwidth. The computing nodes are interconnected with a non-blocking fat-tree using a dual-rail Mellanox EDR InfiniBand interconnect with a total bandwidth of 25GB/s.

In this paper, we use the MPI+CUDA programming model. In all GPU tests, we use 6 MPI tasks per computing node (3 MPI tasks per socket to fully take advantage of both CPU-GPU affinity and network adapter), and each MPI task is bound to an individual GPU. For the comparison of the numerical performance, the CPU version of PWDFT only uses the CPU part of the machine. In the CPU tests, we use the maximum number of cores allowed by PWDFT. Due to the hybrid parallelization scheme, the maximum number of CPU cores is the number of wavefunctions. In the case of 1536 atom silicon system with 3072 wavefunctions, we find that the CPU version of the PWDFT efficiently scales up to 3072 CPU cores.

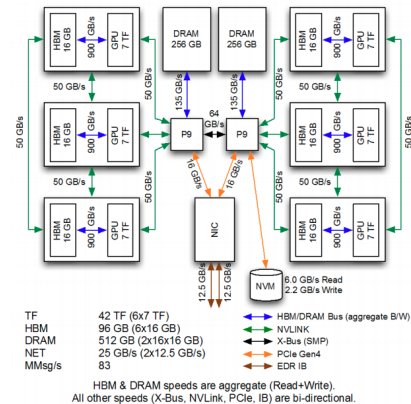


Figure 5: The architecture of a computational node on Summit.

6 NUMERICAL RESULTS

First, we demonstrate the efficiency of the PT-CN algorithm by comparing it to the explicit Runge-Kutta 4th order (RK4) integrator

for the system with 1536 silicon atoms. The time step for PT-CN is set to 50 as and the time step for RK4 is 0.5 as. This is close to the largest time step allowed by RK4 due to the stability constraint. In Fig. 6, we compare the wall clock time for a 50 as simulation using PT-CN and RK4. The PT-CN method can be about 20 times faster compared to the explicit time integrator RK4 method using 36 GPUs, and becomes 30 times faster when using 768 GPUs. The increase of the speedup factor with respect to the number of GPUs is mainly due to that PT-CN can use a larger step size, and is less impacted by the cost of “others” component in section 3.4 (such as the evaluation of the Hartree potential). A detailed discussion of the scaling of different components will be presented in section 7.

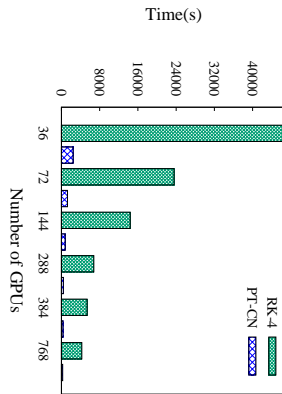
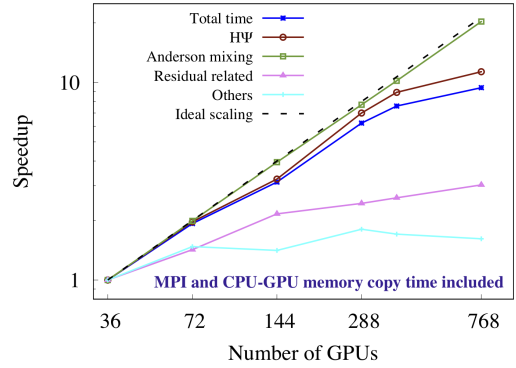


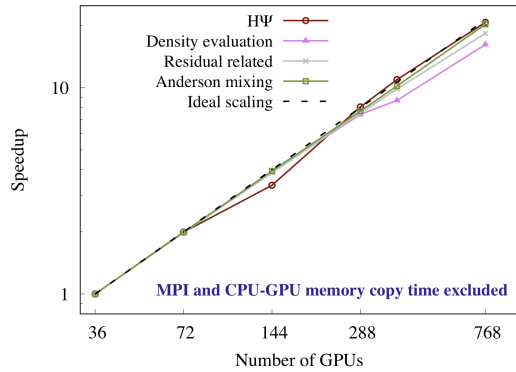
Figure 6: Wall clock time for simulating the 1536 silicon atom system for 50 attoseconds using RK4 and PT-CN methods.

Second, we compare the performance of the GPU version of PWDFT with the CPU one. One of the most important criteria in high performance computing, especially in the upcoming exascale era, is power consumption. The power consumption of a single POWER 9 socket is 190 watt and that of a single NVIDIA V100 GPU is 300 watt. Hence the power cost for each CPU node consisting of 2 POWER 9 CPU sockets is 380 watt and each GPU computing node with 6 V100 GPUs and 2 POWER 9 CPU sockets is 2180 watt. Using 3072 CPU cores (in practice using 73 computing nodes), the total power consumption is 27740 watt. The power consumption of 12 GPU nodes is 26160 watt, which consumes slightly less energy than 73 CPU nodes. According to Table 1, in this setup, the GPU version of PWDFT is still 7 times faster compared to the CPU version.

While the CPU version of PWDFT has reached its scaling limit, the GPU version can still scale beyond 72 GPUs. Fig. 7(a) demonstrates the strong scaling of the wall clock time with respect to the number of GPUs. We find that our GPU implementation can scale to 768 GPUs, and near ideal scaling is achieved when the GPU number is less than 384. After 768 GPUs, the MPI communication dominates the computational cost, which prevents the code to scale to a larger number of GPUs. According to Table 1, the GPU version is 34 times faster than the CPU version using 3072 CPU cores. We



(a)



(b)

Figure 7: Strong scaling: (a) Scaling of the total computation time and different components (MPI and CPU-GPU memory copy time included). (b) Scaling of different components (MPI and CPU-GPU memory time excluded). The wall clock time with 36 GPUs is set as the baseline, which is already 3.7 times faster than the CPU version with 3072 CPU cores.

remark that the strong scaling determines the time to solution, and thus is crucially important in practical calculations. Using the GPU version of PWDFT, we can achieve 260 seconds per TDDFT step (50 attoseconds), which amounts to about 1.5 hours per femtosecond for the 1536 silicon atoms system.

The weak scaling using PT-CN method for simulating systems consisting of 48 to 1536 atoms for 50 as is shown in Fig. 8. The number of GPUs is set to $\frac{1}{2}N_{atom}$. The GPU version of PWDFT exhibits excellent weak scaling property. Since the computational complexity of hybrid functional rt-TDDFT simulation scales as $O(N_{atom}^3 \log N_{atom})$, the ideal scaling should be $O(N_{atom}^2)$ as in Fig. 8, neglecting the logarithmic factor. We find that for small

systems, thanks to GPU acceleration, the Fock exchange operator applications has not yet dominated the computational cost, and hence our implementation scales even better than that indicated by the ideal scaling. Even with the system size increases to 1536 atoms, the weak scaling is still very close to the ideal scaling.

Here for a smaller system with 192 atoms, the simulation of 50 as with 96 GPUs is only 16 seconds. This means that each femtosecond simulation takes around 5 minutes. Even a picosecond rt-TDDFT simulation with hybrid functionals is now within reach and would take approximately 4 days.

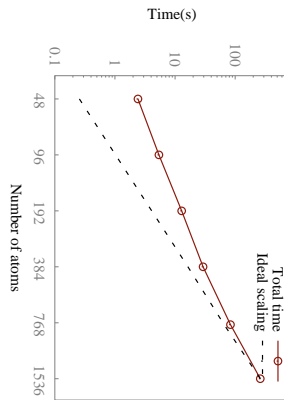


Figure 8: Weak scaling: wall clock time per 50 as for silicon systems with 48 to 1536 atoms. The number of GPUs used are always set to half of number of atoms in the calculation. The “ideal scaling” here scales as $O(N_{atom}^2)$.

7 PERFORMANCE ANALYSIS

In this section, we present a more detailed analysis of the performance of our GPU implementation.

First, we discuss the memory usage of the PT-CN method. In the GPU version of PWDFT, the most memory demanding part is the Anderson mixing, which requires up to 20 copies of wavefunction Ψ . For the system with 1536 atoms, each wavefunction takes 10MB ($N_G = 648,000$ multiplied by the cost of a complex number in double precision format). Using 36 GPUs, each MPI holds less than 100 wavefunctions (1GB). Then Anderson mixing requires less than 20 GB memory per MPI. There are 6 MPIs per computing node, and the total usage of the CPU main memory per node is less than 120GB, which is smaller than the limit of a node on Summit (512GB). Hence our implementation of PT-CN effectively takes advantage of the fat node configuration.

The total number of double precision floating point operations (FLOP) for the 1536 silicon system per TDDFT step is 3.87×10^{16} . This is collected via the CUDA profiling tool NVPROF. Although NVPROF only collects the total number of FLOP on the GPUs, in our implementation the CPU is only responsible for computing quantities labeled as “others” as in section 3.4. The floating point operations per second (FLOPS) is then calculated as $\frac{\text{total FLOP}}{(\text{number of GPUs}) \times (\text{total time})}$,

and the corresponding FLOPS efficiency is $\frac{\text{FLOPS}}{7.8 \text{ TFLOPS}}$. The efficiency of GPU version of PWDFT is 5.5% when using 36 GPUs, and goes down to 2% using 768 GPUs. The low FLOPS efficiency of GPU version of PWDFT is mainly caused by the fact that most FLOP is contributed by the FFTs in Fock exchange operator calculation. The FFT operations on GPU is mainly limited by the CPU-GPU bandwidth rather than the computational kernel. For instance, we find that CUFFT execution reaches about 11% of the peak performance of the V100 GPU in our implementation, and the result is comparable to the performance of CUFFT reported by NVIDIA [26]. The above analysis can be supported by evaluating the average required bandwidth of CUFFT and CUDA custom kernels during the Fock exchange operator calculation. We find that the GPU version of PWDFT achieves approximately 90% of the GPU maximum bandwidth in all tests. Such high GPU memory bandwidth utilization indicates that our calculation is mainly bounded by the hardware memory bandwidth, rather than the FLOPS.

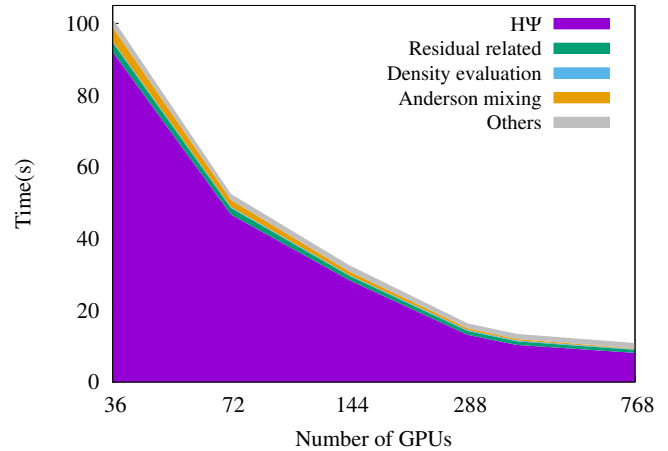


Figure 9: The total time of a single SCF step and the contributions of each part using different number of GPUs.

The total time of a single SCF step can be divided into 5 parts: $H\Psi$, Anderson mixing, the residual related part, the electron density evaluation, and others. The contributions of each part to the total time is listed in Table 1 and shown in Fig. 9. The scaling of different computational components of the GPU version of PWDFT is shown in Fig. 7(a). Since the total computation time is dominated by the application of the Fock exchange operator, the scaling of $H\Psi$ is similar to that of the total time. In each TDDFT step, 24 Fock exchange operator evaluation is performed (22 in the SCF calculation, one in total energy evaluation, and one before SCF calculation to evaluate the residual term R_n), and this contributes to 93% of the total FLOP. The Anderson mixing step scales well with respect to the number of GPUs. The residual related part also scales with the number of GPUs. Its scaling is mainly limited by the MPI_Alltoallv and MPI_Allreduce operations. The “others” components as in section 3.4 are all parallelized on CPUs. As shown in Fig. 9, “others” does not scale with the number of GPUs. It contributes 2.6% of the

total time of a single SCF when using 36 GPUs, and grows up to 15% when using 768 GPUs. Such scaling behavior is mainly caused by the fact that “others” is dominated by the MPI communication of the density related variables using MPI_Bcast.

Next, we discuss the scalability of different computational components in Fig. 7(b). Note that no MPI communication or CPU-GPU memory copy time is included in this figure. We find that nearly all computational time scale well with respect to the number of GPUs. The only computational part that does not scale is the Cholesky decomposition used in the orthogonalization and it is not shown in Fig. 7(b). This part only takes 0.017s on GPU for the 1536 atom system and is calculated once every TDDFT step. Thus it is negligible in the rt-TDDFT calculation. The scaling of the computational time clearly shows that the scaling bottleneck is not the computation. Therefore the main bottleneck comes from the data moment operations, which include both the CPU-GPU memory copy and the MPI communication.

The breakdown of the wall clock time in terms of the MPI communication, CPU-GPU memory copy and computation shown in Fig. 10. The detailed numbers are reported in Table 2. Since memory copies are mostly performed over wavefunctions within each node, the CPU-GPU memory copy operations scale well with respect to the number of GPUs. The MPI_Alltoallv operations is mainly used in the hybrid parallelization scheme to convert the distribution formats of wavefunctions, and is also found to be scalable. The MPI_Allgather operation is performed after the exchange-correlation potential is calculated via Libxc [23]. It contributes less than 0.6% of total time and is thus negligible. The MPI_Bcast operation is mainly used in the Fock exchange operator to broadcast one wavefunction to all GPUs. The MPI_Allreduce operation is performed for computing the charge density and to compute the overlap matrix. These two components are the communication bottleneck. We notice that in our testing results, there are some fluctuations in terms of the communication time in Table 2. For example, the time for MPI_Allreduce peaks at around 288 and 384 GPUs, and the time for MPI_Alltoallv has a local peak at 768 GPUs. We confirm that such fluctuation can be repeatedly observed on Summit with the same configuration, and would like to investigate the origin of such fluctuation in the future.

Let us now analyze the performance of MPI_Bcast from the receiving side. In the Fock exchange operator calculation, each node receives 3072 wavefunctions. Each wavefunction consists of $N_G = 648,000$ complex numbers, which is 5.0MB in the single precision format. Thus total communication volume is $3072 \times 5.0MB = 15.36GB$. The communication time without overlapping with computation is about 7 seconds with 768 GPUs, thus the MPI communication speed is $15.36GB/7s = 2.2 GB/s$. The Summit supercomputer has two NICs connecting to two POWER 9 sockets, respectively. The communication bandwidth for each NIC is 12.5 GB/s. Since we have three MPI tasks per socket, the network bandwidth utilization rate is about 52.7% ($3 \times 2.2/12.5$) from the receiving side. In the GPU version of PWDFT, the CPU MPI_Bcast operation is overlapped with the GPU computation, and the MPI time shown at Table 1 is part of the total communication time. For example, in the 768 GPU case, almost half of the MPI communication time is overlapped by the computation time. Besides the wavefunction MPI_Bcast, we also have the MPI_Bcast of the gradient of charge density, etc. Data

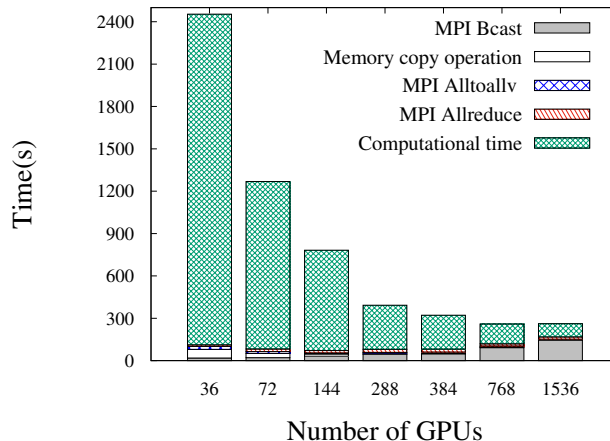


Figure 10: Strong scaling of different operations: MPI communication, CPU-GPU memory copy operation and computation.

size of the charge density is 40MB and it is also network bandwidth limited. The MPI_Allreduce operation is mainly used to evaluate the overlap matrix and charge density. Both operations are performed around 24 times in a single TDDFT step. The data size of the overlap matrix and the charge density vector are 144 MB and 40 MB, respectively. Hence the total data size for MPI_Allreduce is 4.4 GB per time step. This is less than the communication cost of MPI_Bcast but is of the same order of magnitude.

8 CONCLUSION

In this paper, we presented the GPU version of PWDFT for performing rt-TDDFT calculations with hybrid exchange-correlation functional. Our implementation is based on the planewave discretization and the parallel transport (PT) formulation. The PT formulation is used to increase the size of the time step, and therefore reduces the frequency of the Fock exchange operator applications. The multi-GPU implementation reduces the time for applying the Fock exchange operator, as well as other computationally intensive components in rt-TDDFT calculations. This is achieved by carefully rewriting all computational intensive parts with CUDA, and by other techniques to reduce the MPI communication time in the heterogeneous environment. The performance is demonstrated on the Summit supercomputer, and the main techniques can be transferred to other rt-TDDFT as well as ground state DFT software packages. We also found that on the scalability is mainly limited by the network bandwidth on the Summit supercomputer. Hence we expect the parallel performance could scale further with improved network bandwidth on future supercomputers.

ACKNOWLEDGMENTS

This work was partially supported by the National Science Foundation under Grant No. 1450372, No. DMS-1652330 (W. J. and L. L.), and by the Department of Energy under Grant No. DE-SC0017867 (L. L.),

Table 1: Wall clock time of the computationally intensive components for calculating a 1536 silicon atom system. The speedup factor is based on the best CPU implementation with 3072 CPU cores using about 73 computing nodes, and the wall clock time is 8874s.

Number of GPUs	36	72	144	288	384	768	1536	3072
Fock exchange operator MPI	0.71	0.89	1.25	1.83	1.99	3.72	6.06	8.074
Fock exchange operator computaion	90.99	45.61	27.05	11.27	8.31	4.38	2.44	1.43
Fock exchange operator total time	91.7	46.5	28.3	13.1	10.3	8.1	8.5	9.5
Local and semi-local part	0.337	0.169	0.087	0.043	0.0316	0.0158	0.00805	0.00404
$H\Psi$ total time	92.04	46.67	28.39	13.14	10.33	8.12	8.51	9.50
Wavefunction MPI_Alltoallv	0.884	0.561	0.313	0.227	0.212	0.280	0.095	0.056
$\langle\Psi \Psi\rangle$ MPI_Allreduce	0.354	0.593	0.552	0.676	0.667	0.523	0.522	0.5243
Computation	1.43	0.72	0.37	0.19	0.145	0.078	0.04	0.023
Residual related total time	2.67	1.87	1.24	1.09	1.02	0.88	0.66	0.60
CPU-GPU memory copy	1.64235	0.8004	0.4094	0.2018	0.1477	0.0746	0.0395	0.0202
Computation time	2.3	1.16	0.59	0.31	0.265	0.142	0.073	0.04
Anderson mixing total time	3.94	1.98	1.00	0.51	0.387	0.194	0.102	0.0553
Computation time	0.1349	0.0672	0.0341	0.0170	0.0124	0.0062	0.0032	0.0016
MPI_Allreduce	0.123	0.176	0.152	0.224	0.219	0.160	0.164	0.171
Density evaluation total time	0.258	0.243	0.186	0.241	0.232	0.167	0.167	0.172
Others	2.66	1.98	1.72	1.54	1.57	1.73	1.66	1.85
per SCF time	101.36	52.4	32.5	16.4	13.4	10.9	10.9	12.1
Total time	2453.8	1269.1	783.0	393.9	323.2	260.9	262.5	286.6
Total speedup	3.6x	7.0x	11.3x	22.5x	27.4x	34x	33.8x	30.9x
$H\Psi$ percentage	90%	88.3%	87%	80%	76.7%	74.6%	77.8%	79.6%

Table 2: Breakdown of the total time into the time for MPI, CPU-GPU memory copy and computation. The CPU-GPU memory copy time and MPI time are all gathered in the runtime phase, the computational time is calculated by removing all the communication time from the total time in Table 1.

Number of GPUs	36	72	144	288	384	768	1536	3072
CPU-GPU memory copy time	60.80	29.94	16.04	8.57	6.79	4.15	2.82	2.24
MPI_Alltoallv time	20.97	13.34	7.40	5.38	4.99	6.64	2.41	0.68
MPI_Allreduce time	11.50	18.39	16.70	21.27	21.15	16.19	16.44	16.62
MPI_Bcast time	18.78	20.89	31.06	44.54	48.13	92.26	146.15	193.89
MPI_AllGatherv time	0.44	1.12	1.30	1.35	1.52	1.38	0.98	1.24
MPI total time	51.69	53.74	56.45	72.54	75.79	116.47	165.97	212.43
Computational time	2341.40	1185.42	710.54	312.83	240.60	140.34	93.73	71.96

and by the Department of Energy Theory of Materials (KC2301) program under Contract No. DE-AC02-05CH11231 (L. W.). We thank the Oak Ridge National Laboratory leadership computing facility for making the computational resources available. We thank Zhanghui Chen and Mauro Del Ben for helpful discussions.

REFERENCES

- [1] D. An and L. Lin. [n. d.]. Quantum dynamics with the parallel transport gauge. *arXiv:1804.02095* [n. d.].
- [2] D. G. Anderson. 1965. Iterative procedures for nonlinear integral equations. *J. Assoc. Comput. Mach.* 12 (1965), 547–560.
- [3] Xavier Andrade, Joseba Alberdi-Rodriguez, David A Strubbe, Micael J T Oliveira, Fernando Nogueira, Alberto Castro, Javier Muguerza, Agustin Arruabarrena, Steven G Louie, Alan Aspuru-Guzik, Angel Rubio, and Miguel A L Marques. 2012. Time-dependent density-functional theory in massively parallel computer architectures: the octopus project. *J. Phys. Condens. Matter* 24 (2012), 233202.
- [4] Xavier Andrade, Joseba Alberdi-Rodriguez, David A Strubbe, Micael J T Oliveira, Fernando Nogueira, Alberto Castro, Javier Muguerza, Agustin Arruabarrena, Steven G Louie, Alan Aspuru-Guzik, Angel Rubio, and Miguel A L Marques. 2012. Time-dependent density-functional theory in massively parallel computer architectures: the octopus project. *Journal of Physics: Condensed Matter* 24, 23 (may 2012), 233202. <https://doi.org/10.1088/0953-8984/24/23/233202>
- [5] A. D. Becke. 1993. Density functional thermochemistry. III. The role of exact exchange. *J. Chem. Phys.* 98 (1993), 5648.
- [6] I. Carnimeo, S. Baroni, and P. Giannozzi. 2018. Fast hybrid density-functional computations using plane-wave basis sets. *Electronic Structure* (2018).
- [7] A. Damle, L. Lin, and L. Ying. 2015. Compressed Representation of Kohn–Sham Orbitals via Selected Columns of the Density Matrix. *J. Chem. Theory Comput.* 11, 4 (2015), 1463–1469.
- [8] W. Dawson and F. Gygi. 2015. Performance and Accuracy of Recursive Subspace Bisection for Hybrid DFT Calculations in Inhomogeneous Systems. *J. Chem. Theory Comput.* 11 (2015), 4655–4663.
- [9] I. Duchemin and F. Gygi. 2010. A scalable and accurate algorithm for the computation of Hartree–Fock exchange. *Comput. Phys. Commun.* 181 (2010), 855–860.
- [10] J. Fattebert, D. Osei-Kuffuor, E. W. Draeger, T. Ogitsu, and W. D. Krauss. 2016. Modeling Dilute Solutions Using First-Principles Molecular Dynamics: Computing more than a Million Atoms with over a Million Cores. In *SC'16: Proceedings of the International Conference for High Performance Computing, Networking, Storage and Analysis*. 12–22. <https://doi.org/10.1109/SC.2016.88>
- [11] X. Gonze, F. Jollet, F. Abreu Araujo, D. Adams, B. Amadon, T. Applencourt, C. Audouze, J.-M. Beuken, J. Bieder, A. Bokhanchuk, E. Bousquet, F. Bruneval, D. Caliste, M. Caftal, F. Dahm, F. Da Pieve, M. Delaveau, M. Di Gennaro, B.

- Dorado, C. Espejo, G. Geneste, L. Genovese, A. Gerossier, M. Giantomassi, Y. Gillet, D.R. Hamann, L. He, G. Jomard, J. Laflamme Janssen, S. Le Roux, A. Levitt, A. Lherbier, F. Liu, I. Lukačević, A. Martin, C. Martins, M.J.T. Oliveira, S. Poncá, Y. Pouillon, T. Rangel, G.-M. Rignanes, A.H. Romero, B. Rousseau, O. Rubel, A.A. Shukri, M. Stankovski, M. Torrent, M.J. Van Setten, B. Van Troeye, M.J. Verstraete, D. Waroquiers, J. Wiktor, B. Xu, A. Zhou, and J.W. Zwanziger. 2016. Recent developments in the ABINIT software package. *Computer Physics Communications* 205 (2016), 106 – 131. <https://doi.org/10.1016/j.cpc.2016.04.003>
- [12] Mohamed Hacene, Ani Anciaux-Sedrakian, Xavier Rozanska, Diego Klahr, Thomas Guignon, and Paul Fleurat-Lessard. 2012. Accelerating VASP electronic structure calculations using graphic processing units. *Journal of computational chemistry* 33, 32 (2012), 2581–2589.
- [13] D. R. Hamann. 2013. Optimized norm-conserving Vanderbilt pseudopotentials. *Phys. Rev. B* 88 (2013), 085117.
- [14] J. Heyd, G. E. Scuseria, and M. Ernzerhof. 2003. Hybrid functionals based on a screened Coulomb potential. *J. Chem. Phys.* 118, 18 (2003), 8207–8215.
- [15] J. Heyd, G. E. Scuseria, and M. Ernzerhof. 2006. Erratum: “Hybrid functionals based on a screened Coulomb potential” [*J. Chem. Phys.* 118, 8207 (2003)]. *J. Chem. Phys.* 124, 21 (2006), 219906.
- [16] W. Hu, L. Lin, and C. Yang. 2015. DGDFT: A massively parallel method for large scale density functional theory calculations. *J. Chem. Phys.* 143 (2015), 124110.
- [17] W. Hu, L. Lin, and C. Yang. 2017. Interpolative separable density fitting decomposition for accelerating hybrid density functional calculations with applications to defects in silicon. *J. Chem. Theory Comput.* 13 (2017), 5420.
- [18] Maxwell Hutchinson and Michael Widom. 2012. VASP on a GPU: Application to exact-exchange calculations of the stability of elemental boron. *Computer Physics Communications* 183, 7 (2012), 1422–1426.
- [19] W. Jia, D. An, L.-W. Wang, and L. Lin. [n. d.]. Fast real-time time-dependent density functional theory calculations with the parallel transport gauge. *arXiv:1805.10575* [n. d.].
- [20] Weile Jia, Zongyan Cao, Long Wang, Jiyun Fu, Xuebin Chi, Weiguo Gao, and Lin-Wang Wang. 2013. The analysis of a plane wave pseudopotential density functional theory code on a GPU machine. *Computer Physics Communications* 184, 1 (2013), 9 – 18. <https://doi.org/10.1016/j.cpc.2012.08.002>
- [21] Weile Jia, Jiyun Fu, Zongyan Cao, Long Wang, Xuebin Chi, Weiguo Gao, and Lin-Wang Wang. 2013. Fast plane wave density functional theory molecular dynamics calculations on multi-GPU machines. *J. Comput. Phys.* 251 (2013), 102 – 115. <https://doi.org/10.1016/j.jcp.2013.05.005>
- [22] Weile Jia and Lin Lin. 2019. Fast real-time time-dependent hybrid functional calculations with the parallel transport gauge and the adaptively compressed exchange formulation. *Computer Physics Communications* (2019). <https://doi.org/10.1016/j.cpc.2019.02.009>
- [23] Susi Lehtola, Conrad Steigemann, Micael J.T. Oliveira, and Miguel A.L. Marques. 2018. Recent developments in libxc: A comprehensive library of functionals for density functional theory. *SoftwareX* 7 (2018), 1 – 5. <https://doi.org/10.1016/j.softx.2017.11.002>
- [24] L. Lin. 2016. Adaptively Compressed Exchange Operator. *J. Chem. Theory Comput.* 12 (2016), 2242.
- [25] L. Lin, J. Lu, L. Ying, and W. E. 2012. Adaptive local basis set for Kohn-Sham density functional theory in a discontinuous Galerkin framework I: Total energy calculation. *J. Comput. Phys.* 231 (2012), 2140–2154.
- [26] NVIDIA. [n. d.]. CUDA 8 Performance Overview. ([n. d.]). <http://developer.download.nvidia.com/compute/cuda/compute-docs/cuda-performance-report.pdf>
- [27] G. Onida, L. Reining, and A. Rubio. 2002. Electronic excitations: density-functional versus many-body Green’s-function approaches. *Rev. Mod. Phys.* 74 (2002), 601.
- [28] J. P. Perdew, M. Ernzerhof, and K. Burke. 1996. Rationale for mixing exact exchange with density functional approximations. *J. Chem. Phys.* 105 (1996), 9982–9985.
- [29] Laura E Ratcliff, A Degomme, José A Flores-Livas, Stefan Goedecker, and Luigi Genovese. 2018. Affordable and accurate large-scale hybrid-functional calculations on GPU-accelerated supercomputers. *Journal of Physics: Condensed Matter* 30, 9 (feb 2018), 095901. <https://doi.org/10.1088/1361-648x/aaa8c9>
- [30] Joshua Romero, Everett Phillips, Gregory Ruetsch, Massimiliano Fatica, Filippo Spiga, and Paolo Giannozzi. 2018. A Performance Study of Quantum ESPRESSO’s PWscf Code on Multi-core and GPU Systems. In *High Performance Computing Systems. Performance Modeling, Benchmarking, and Simulation*, Stephen Jarvis, Steven Wright, and Simon Hammond (Eds.). Springer International Publishing, Cham, 67–87.
- [31] E. Runge and E. K. U. Gross. 1984. Density-functional theory for time-dependent systems. *Phys. Rev. Lett.* 52 (1984), 997.
- [32] M. Schlipf and F. Gygi. 2015. Optimization algorithm for the generation of ONCV pseudopotentials. *Comput. Phys. Commun.* 196 (2015), 36–44.
- [33] C. A. Ullrich. 2011. *Time-dependent density-functional theory: concepts and applications*. Oxford Univ. Pr.
- [34] M. Valiev, E.J. Bylaska, N. Govind, K. Kowalski, T.P. Straatsma, H.J.J. Van Dam, D. Wang, J. Nieplocha, E. Apra, T.L. Windus, and W.A. de Jong. 2010. NWChem: A comprehensive and scalable open-source solution for large scale molecular simulations. *Computer Physics Communications* 181, 9 (2010), 1477 – 1489. <https://doi.org/10.1016/j.cpc.2010.04.018>
- [35] M. Valiev, E. J. Bylaska, N. Govind, K. Kowalski, T. P. Straatsma, H. J. J. Van Dam, D. Wang, J. Nieplocha, E. Apra, T. L. Windus, and W. De Jong. 2010. NWChem: a comprehensive and scalable open-source solution for large scale molecular simulations. *Comput. Phys. Commun.* 181 (2010), 1477–1489.
- [36] Long Wang, Yue Wu, Weile Jia, Weiguo Gao, Xuebin Chi, and Lin-Wang Wang. 2011. Large Scale Plane Wave Pseudopotential Density Functional Theory Calculations on GPU Clusters. In *Proceedings of 2011 International Conference for High Performance Computing, Networking, Storage and Analysis (SC ’11)*. ACM, New York, NY, USA, Article 71, 10 pages. <https://doi.org/10.1145/2063384.2063479>
- [37] Lin-Wang Wang. 2001. Mask-function real-space implementations of nonlocal pseudopotentials. *Phys. Rev. B* 64 (Nov 2001), 201107. Issue 20. <https://doi.org/10.1103/PhysRevB.64.201107>
- [38] X. Wu, A. Selloni, and R. Car. 2009. Order-N implementation of exact exchange in extended insulating systems. *Phys. Rev. B* 79, 8 (2009), 085102.
- [39] K. Yabana and G. F. Bertsch. 1996. Time-dependent local-density approximation in real time. *Phys. Rev. B* 54 (1996), 4484–4487.